Title

Physical Principles of Multibeam Sonar for Mapping of the Seafloor

Authors

Sandwell, David

DeSanto, John

Publication Date

2023-12-14

DOI

10.13140/RG.2.2.27027.96805

Physical Principles of Multibeam Sonar for Mapping of the Seafloor

John DeSanto and David Sandwell

February 24, 2022

1 Introduction

A multibeam sonar mounted on the hull of a large research vessel provides an important tool for mapping the seafloor in the deep ocean at moderate spatial resolution and accuracy (Figure 1). This document provides a very brief introduction into the physical principles of a particular multibeam echo sounder that is able to map in the deepest ocean at approximately 100 m spatial resolution. The overall geometry is shown in Figure 1. The ship cruises along the surface of the ocean at a speed typically less than 12 knots (i.e. 6 m/s). It emits a sonar signal from hull-mounted transducers. These acoustic waves reflect from the seafloor and return to the ship mapping out a swath of seafloor 3-4 times the ocean depth. Some basic references for the method and technology are Farr [1980], de Moustier [1988], and Kongsberg [2011].

The sonar elements are mounted in a gondola or pod (Figure 2) that is fastened to the deepest part of the hull of the ship where it will remain submerged even in rough seas. The sonar consists of two arrays. Sound pulses are generated by a 7 m long array of transducers that are oriented parallel to the keel of the ship (Figure 2, EM122 TX). The return echoes are recorded in a 7 m long array of hydrophones oriented perpendicular to the keel of the ship (Figure 2, EM122 RX). In this short document we'll try to answer some basic questions such as: Why are the transmit and receive arrays so long? Why are they arranged in a T structure? Since the gondola is fixed to the hull of the ship, what happens when the ship undergoes yaw, pitch, and roll motions. The first part of the document will be related to

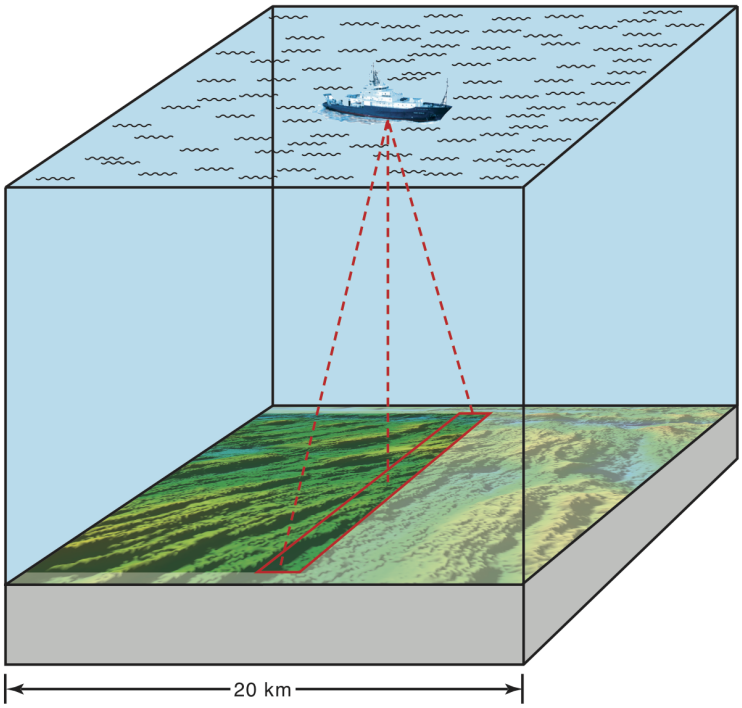

Figure 1: Schematic diagram of a multibeam echo sounder mapping a swath of seafloor.

some basic physical principles of sonar propagation in seawater and beam forming. These physical limitations guide the overall design and limitations of the multibeam approach for seafloor mapping. What is missing from this document is a description of the marvelous and sophisticated engineering that has gone into the development and refinement of these systems.

Much of the physics of multibeam sonar is similar to radar interferometry mapping of topography by satellites. The major difference is that satellites provide a very stable platform where the position and orientation vary smoothly with time, so the motion compensation corrections are simple and accurate. In contrast, the ship is constantly undergoing extreme motions and rotations at periods that are shorter than the two-way travel time of the

Figure 2: Gondola containing a 7 m long array of transducers (EM122 TX) that are oriented parallel to the keel of the ship and a 7 m long array of hydrophones (EM122 RX) perpendicular to the keel. This system is a Kongsberg EM122 multibeam sonar being mounted on the hull of the RV Langseth. (Photo credit, John Greene, Texas A&M).

sonar echoes. The compensation for these motions is easy to understand from a physical perspective (this document) but enormously challenging from an engineering perspective.

2 Mapping Geometry

The objective is to measure ocean depth in a swath perpendicular to the track of the ship – one cross-track profile for each ping of the sonar. The geometry is illustrated in Figure 3 where the ship is on the ocean surface and moving into the page. Consider a sound pulse that is emitted from the hull at a look angle of θ from the vertical. The pulse travels at the speed of sound C along the ray path labeled ρ. It reflects from the seafloor and returns to the ship. The range is estimated from the two-way travel time Δt as $\rho = \Delta t c$. The estimated depth at that location is $H(\theta) = \rho / \cos\theta$. Therefore in addition to

the range measurement, the look angle of the return pulse must be accurately estimated. We will discuss the principles and limitations of forming a narrow sonar beam in the next section.

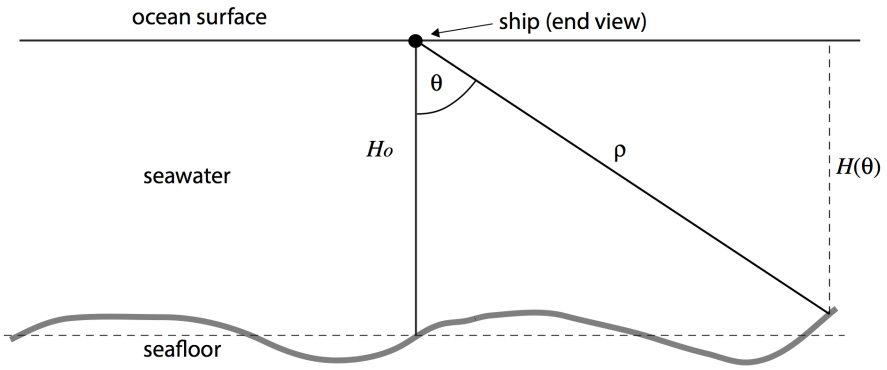

Figure 3: Schematic diagram of a ray of sound energy, emitted at a look angle of θ, from a ship moving into the page. H_0 is the depth directly beneath the ship at zero look angle. The off-nadir depth is $H(\theta) = \rho / \cos\theta$.

The maximum look angle of this mapping is limited by three effects. (1) First the outgoing pulse will not send all of its energy in the look direction and some fraction will be emitted in the vertical direction through a sidelobe of the sonar beam (discussed below). The backscattered energy is highest at a vertical look angle so significant energy can come from this nadir reflection but more importantly there will be significant energy in the pulse that has a double bounce. The 2-way travel time of the double bounce is equal to the 2-way travel time of a single reflected pulse at a 60° look angle assuming equal ocean depth at these two locations. Therefore at look angles of 60° and higher the double bounce will arrive at or before the off-nadir reflected pulse and the sonar will have difficulty to uniquely identify the travel time of the main reflection. This limits the swath to about 3.5 times the vertical ocean depth although larger widths are possible with sector illumination techniques discussed below. (2) The second limitation is related to a non-uniform sound velocity in the upper ocean. This will cause the ray path to bend mostly outward (away from the look angle); at extreme look angles approaching 90°, the outgoing ray may never reach the ocean floor. (3) The third limitation is

Table 1: Characteristics of sonar in the ocean.

f - frequency (kHz)	λ - wavelength (m)	α - attenuation distance (km)	wavelength analogy for radar
3.5	0.43	48	P
12	0.13	8	S
30	0.05	2	C
70	0.02	0.7	X

related to the attenuation of the sonar pulse as it passes through the ocean. If the attenuation is very strong then the sonar will not be able to detect energy from the return pulse. This selection of an acceptable sonar frequency for deep ocean mapping is discussed next.

3 Selection of Sonar Frequency

A main objective of this system is to have the ability to map the seafloor at all ocean depths. A significant limitation of sonar is the attenuation of energy as the waves propagate through the ocean. High frequency waves are more strongly attenuated than lower frequency waves as shown in Figure 4. Commonly used sonar frequencies are provided in Table 1 along with the wavelength for a nominal sound speed of 1500 m/s. The table also provides the propagation distance where the waves are attenuated by 1/4 of their initial power [Ainslie and McColm, 1998]. The median ocean depth is about 4 km as illustrated in the hypsometry of the ocean (Figure 5) (e.g., Becker et al. [2009]). The maximum ocean depth in the Mariana trench is about 11 km but most of the seafloor lies at depths less than 6 km. As discussed above the range to the outermost beam having a look angle of 60° is two times the nadir ocean depth. Therefore, a lower frequency sonar (12 kHz) is needed to obtain full swath coverage at the most common 4 km ocean depth and also have the ability to map at 8 km depth with a narrower swath. From this analysis we have constrained the wavelength of our sonar to be longer than about 0.12 m. Next we will see how this effects the ability to focus the sonar beam.

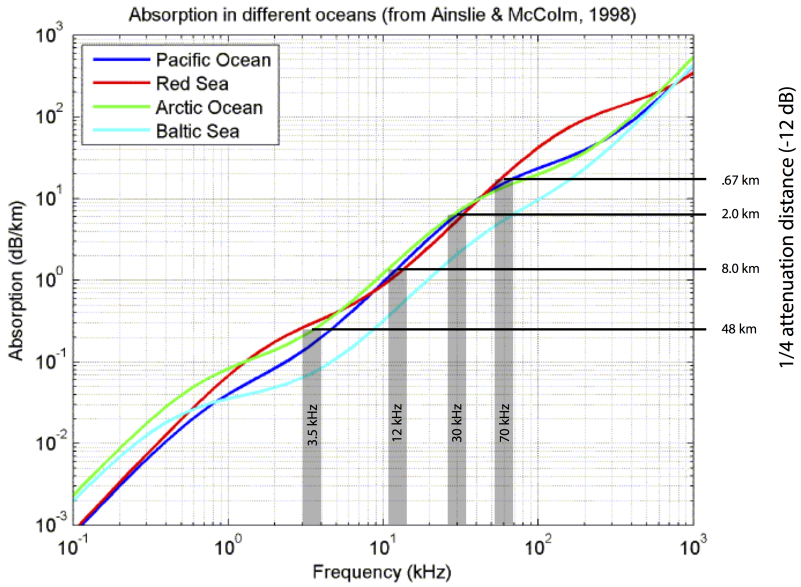

Figure 4: Absorption of sonar power per km of propagation as a function of frequency for several bodies of seawater. The right axis shows the length where the sonar power is attenuated by 1/4. Lower frequency sonars (e.g., 3.5 kHz) can propagate long distances (about 48 km) and retain detectable power while high frequency sonars (e.g., 70 kHz) suffer significant loss over much shorter distances (about 0.67 km) (modified from Ainslie and McColm [1998]).

4 Fraunhoffer Diffraction

The beamwidth of a sonar pulse is governed by the principles of Fraunhoffer diffraction. Consider a coherent sonar pulse generated across an aperture of length L as shown in Figure 6. First we'll consider a 1-D aperture and then go on to a 2-D rectangular aperture to simulate a rectangular array of transducers or hydrophones as shown in Figure 2. The 2-D case provides the shape and dimension of the footprint of the sonar. These notes were developed from Rees [2013] and Bracewell [1986] for electromagnetic radiation but the principles are equivalent for sonar.

We simulate coherent radiation by numerous point sources of sound (trans-

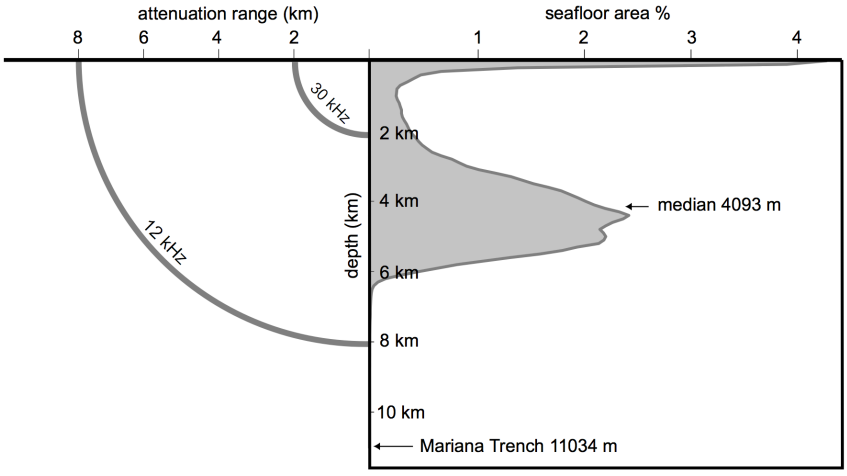

Figure 5: (left) attenuation range for sonar waves in the ocean at 30 kHz and 12 kHz. (right) histogram of area of seafloor as a function of depth. The median ocean depth is about 4 km and most of the ocean is shallower than 8 km. Deep ocean mapping requires lower sonar frequencies (12 kHz).

ducers) distributed along the aperture between $-L/2$ and $L/2$. For simplicity we'll assume all the sources have the same amplitude, wavelength λ, and phase. Given these sources of radiation, we solve for the illumination pattern on the screen as a function of θ. We'll assume that the screen is far enough from the aperture so that rays AP and OP are parallel. Later we'll determine how far away the screen needs to be in order for this approximation to hold. Under these conditions, the ray AP is slightly shorter than the ray OP by an amount $-y \sin\theta$. This corresponds to a phase shift of $\frac{-2\pi}{\lambda} y \sin\theta$. The amplitude of the illumination at point P is the integral over all of the sources along the aperture multiplied by their complex phase value

$$P(\theta) = \int_{-L/2}^{L/2} A(y) e^{-i2\pi y k \sin\theta} dy \tag{1}$$

where $k = 1/\lambda$. This is called the Fraunhoffer diffraction integral. The illumination across the aperture is uniform in both amplitude and phase so we set $A(y) = 1$. Later we'll adjust the phase across the aperture to shift the peak in the energy away from $\theta = 0$. Now let $s = 2\pi k \sin\theta$ so the integral is

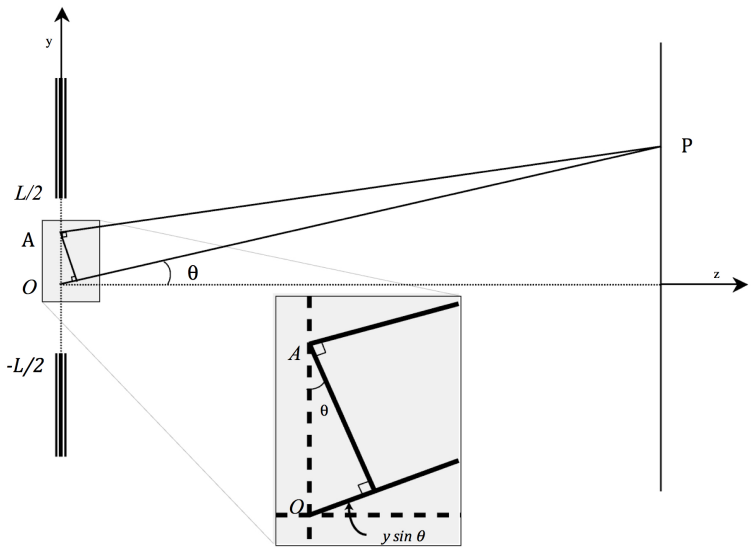

Figure 6: Diagram for the projection of coherent sound waves on a screen (e.g. seafloor) that is far from the aperture of length L.

easy to evaluate.

$$P(s) = \int_{-L/2}^{L/2} e^{-isy} dy = \frac{e^{-isL/2} - e^{isL/2}}{-is} = \frac{2}{s}\sin(sL/2) = L\text{sinc}(sL/2) \quad (2)$$

Replacing s with $2\pi \sin\theta/\lambda$ we arrive at the final result.

$$P(\theta) = L\text{sinc}\left(\frac{L\pi \sin\theta}{\lambda}\right) \quad (3)$$

The illumination pattern on the screen is shown in Figure 7 (solid curve).

The first zero crossing, or angular resolution θ_r of the sinc function occurs when the argument is π so

$$\sin\theta_r = \lambda/L. \quad (4)$$

At this point it is instructive to calculate the angular resolution of the aperture of the EM122 system shown in Figure 2. The length of this aperture

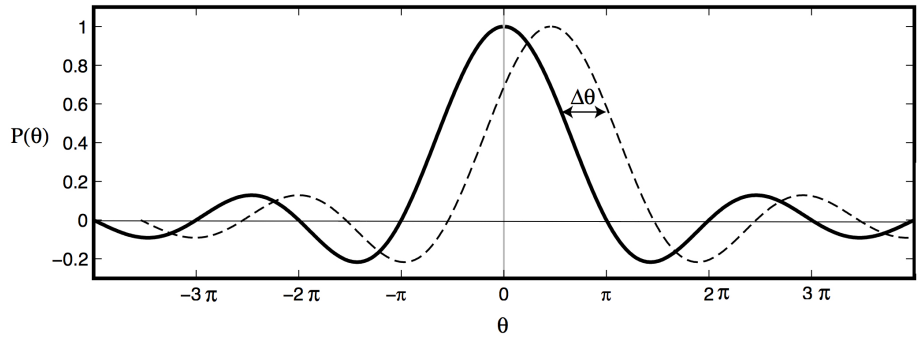

Figure 7: Sinc function illumination pattern for the aperture shown in Figure 6. Solid curve is for uniform phase across the aperture. Dashed curve is for a linear phase ramp across the aperture to shift the location of the peak by $\Delta\theta$.

is 7 m and we use a 0.13 m wavelength sonar to reach full ocean depth. Given these values and equation (4) we find an angular resolution of 1°. If we constructed TX and RX arrays 10 times smaller with an aperture length of say 0.7 m then the angular resolution of the two arrays would be 10°. At an ocean depth of 4 km this would correspond to a spatial resolution of 700 m, which is inadequate for many mapping purposes. Figure 2 also shows the location of a 12 kHz transducer having a diameter of about 0.5 m. This type of transducer would produce a very broad beam that would roughly correspond to the single-beam echo sounders used on research vessels before the multibeam technology was available. So now we have answered the question of why the TX and RX arrays are so long. We need longer wavelength sonar to reach full ocean depth but to resolve features of about 1° the basic physics dictates that the array be approximately 7 meters long. We still have not explained the shorter width of the apertures and their T configuration.

The next modifications to the aperture are to change the amplitude and phase of the transducers (or hydrophones) across the array (i.e., $A(y)$). First, one could modify the amplitude of the illumination across the aperture. For example, a Gaussian aperture would produce a Gaussian illumination function on the screen. This would eliminate the side lobes associated with the sinc function but it would also broaden the projection pattern. Second we could vary the phase of the transponders across the aperture to shift the point of maximum illumination away from $\theta = 0$. We accomplish by a linear

variation phase of the illumination across the aperture given by

$$A(y) = e^{i2\pi yk \sin\theta_0}. \tag{5}$$

In this case the Fraunhoffer diffraction integral becomes

$$P(\theta) = \int_{-L/2}^{L/2} A(y) e^{-i2\pi yk \sin\theta} dy = \int_{-L/2}^{L/2} e^{-i2\pi yk(\sin\theta - \sin\theta_0)} dy. \tag{6}$$

Following the approach above, we integrate and find the result is

$$P(\theta) = L\text{sinc}\left[\frac{L\pi(\sin\theta - \sin\theta_0)}{\lambda}\right]. \tag{7}$$

The peak in the projection pattern is shifted by an amount $\Delta\theta = \sin^{-1}(\sin\theta - \sin\theta_0)$ as shown by the dashed line in Figure 7. This phased array approach is used to form the off-nadir beams across the swath of the multibeam as described below. Moreover it is used to compensate for the pitch of the ship on the outgoing pulse of the transmit array as well as the roll on the incoming wave fronts of the receive array. A diagram of how the look angle of the incoming sonar waves are electronically shifted away from nadir is shown in Figure 8.

Before moving on to the 2-D case, we should check the assumption used in developing the Fraunhoffer diffraction integral that the rays AP and OP are parallel. Suppose we examine the case when $\theta = 0$; the ray path AP is slightly longer than OP (Figure 9). This parallel-ray assumption breaks down when the phase of ray path AP is more than $\pi/2$ radians longer than OP, which corresponds to a distance of $\lambda/4$. Let's determine the conditions when this happens.

The condition that the path length difference is smaller than 1/4 wavelength is

$$\left[\frac{L^2}{4} + z^2\right]^{1/2} - z < \frac{\lambda}{4} \tag{8}$$

or can be rewritten as

$$\left[\left(\frac{L}{2z}\right)^2 + 1\right]^{1/2} - 1 < \frac{\lambda}{4z}. \tag{9}$$

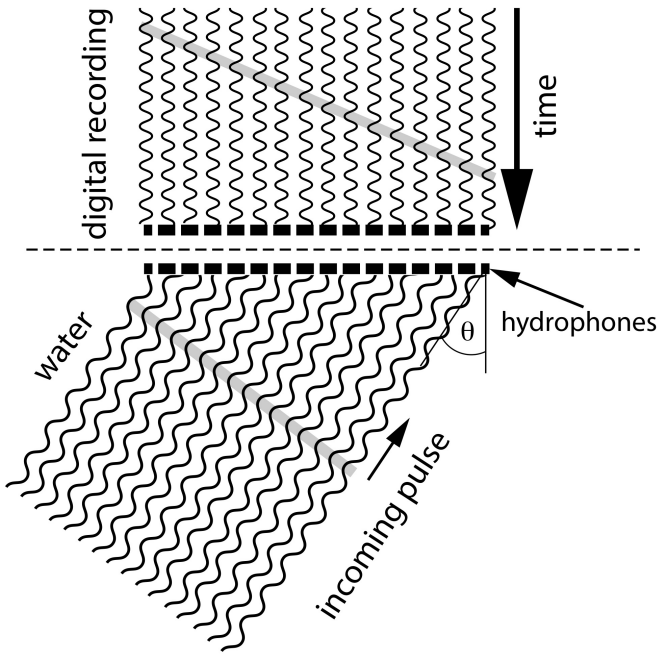

Figure 8: Diagram showing coherent waves from an off-nadir reflection being recorded by an array of hydrophones across an aperture. To extract a time series of the energy arriving from that direction one sums the pulses with an appropriate time delay.

Now assume $L << z$ so we can expand the term in brackets into a binomial series.

$$1 + \frac{L^2}{8z^2} - 1 < \frac{\lambda}{4z} \tag{10}$$

and we find $z_f > \frac{L^2}{2\lambda}$ where z_f is the Fresnel distance. So when $z < z_f$ we are in the near field and we need to use a more rigorous diffraction theory. However when $z >> z_f$ we are safe to use the parallel-ray approximation and the Fraunhoffer diffraction integral is appropriate. As shown in Figure 2, our aperture has a length of 7 m and based on the need for 8 km propagation we have selected a wavelength of 0.13 m. For this case the Fresnel distance is 188 m. We will mainly be using this system to map areas greater than 200

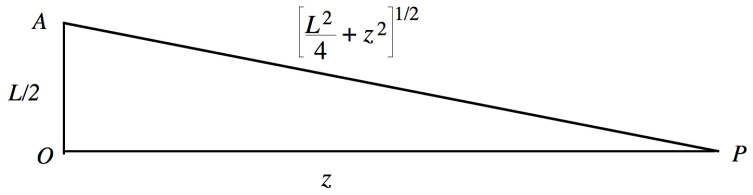

Figure 9: Diagram showing the increases length of path AP with respect to OP due to an offset of $L/2$.

m depth so the parallel ray approximation is valid.

5 2-D Aperture

A 2-D rectangular aperture is a good approximation for both the transmit and receive arrays shown in Figure 2. The transmit aperture is longer in the keel direction (length L) than in the perpendicular direction (width W) as shown in Figure 2. One uses a 2-D Fraunhoffer diffraction integral to calculate the projection pattern of the antenna. The integral is

$$P(\theta_x, \theta_y) = \int_{-L/2}^{L/2} \int_{-W/2}^{W/2} A(x,y) \exp\left[i \frac{2\pi}{\lambda}(x \sin\theta_x + y \sin\theta_y)\right] dxdy \qquad (11)$$

where λ is the wavelength of the radar. As in the 1-D case we'll assume the aperture $A(x, y)$ has uniform amplitude and phase. In this case the projection pattern can be integrated analytically and is

$$P(\theta_x, \theta_y) = LW \text{sinc}\left(\frac{\pi W \sin\theta_x}{\lambda}\right) \text{sinc}\left(\frac{\pi L \sin\theta_y}{\lambda}\right). \qquad (12)$$

The first zero crossing of this 2-D sinc function is illustrated in Figure 10 (right).

6 Mills Cross Configuration

High 2-D resolution of a patch of seafloor can be achieved by setting the transmit array with the long axis along the keel of the ship and the long axis

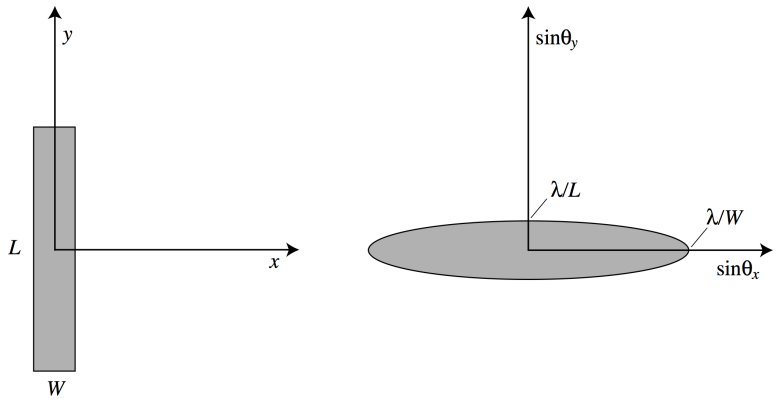

Figure 10: Diagram showing the projection pattern (right) for a rectangular aperture (left).

of the receive array in the perpendicular direction; this is called a mills cross configuration. The beam pattern on the seafloor is shown in Figure 11.

In the case of the Konsberg EM122, the transmit array has a length of 7.8 m and a width of 0.78 m resulting in a 0.92° resolution in the along-track direction and a 9.2° resolution across the track. As discussed above the overall swath width can be 150°, which is significantly wider than the 9.2° cross track angle. Indeed the transmit array has 18 elements along the keel and 6 elements across the keel. The 6 cross-track elements are used to focus the outgoing beam in up to 9 sectors in the cross track direction. Each ping of the sonar actually consists of 9 pings with a slight time and frequency offset to ensonify the entire 150° swath, or whatever swath width was selected by the user. Some examples of the raw stave (i.e. hydrophone) data for the 9 sectors are shown in the next section.

The receive array is 7.2 m in the across-keel directions and 0.42 m along the keel resulting in a cross-track resolution pattern of 0.99° and an along-track resolution of 17.3°. The receive array has 128 hydrophones (or staves) having the ability to record over a wide bandwidth centered at 12 kHz. All 128 staves record the entire time series of reflected waves over a time window beginning at the time the pulse was emitted and ending at the two-way travel time of the most distant reflection at a look angle of up to 75°. After the data

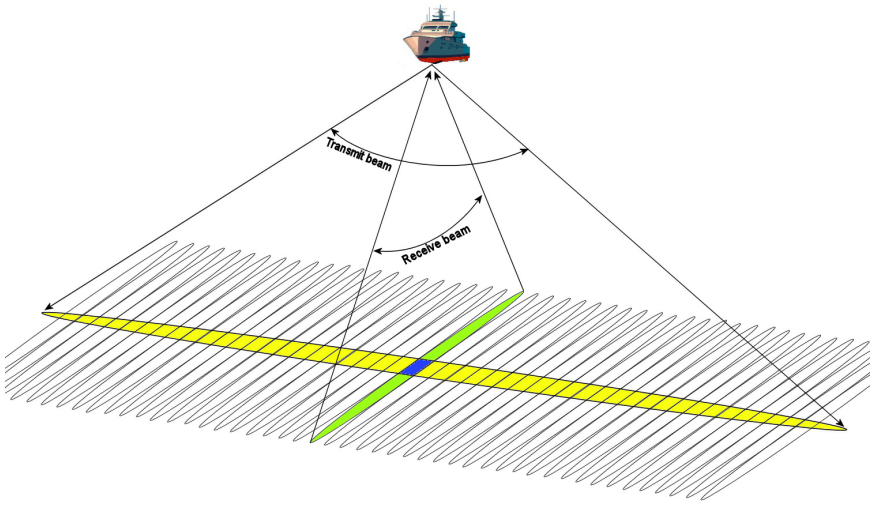

Figure 11: Schematic diagram of the beam patterns of transmit (yellow) and receive (green) arrays on the seafloor. The intersection of the 0° incidence angle receive beam and the transmit beam is shown as a blue box (1°x1°). The other cross-track beams are resolved by synthesizing a non-nadir focus in the computer after the data are collected on all the hydrophones of the receive array.

are recorded, they are first divided into the 9 sectors by frequency filtering and then focussed into cross-track beams by summing with the appropriate time delay. Both operations are performed with the Fast Fourier transform algorithm to speed the processing. An example of the original stave data is shown in Figure 12. This example comes from an EM120 with only 64 staves. The range sampling rate is 2 kHz so the first arrivals are at about 3 seconds corresponding to a depth of 2250 m. Note the nadir double bounce arrives at about 6 seconds. After beamforming (right) the horizontal axis corresponds to the sine of the look angle. The higher look angles have two-way travel times of up to 7 seconds corresponding to a distance of 5250 m. (Note that beamforming is simply the FFT of each row with the output shifted so the lowest wavenumber is in the center of the array and corresponds to the Nadir beam.)

As discussed above, 9 individual pings are emitted for each sonar echo and each of these pings has its own center look angle and center frequency as provided in Table 2. For ocean depths greater than 2000 m the bandwidth

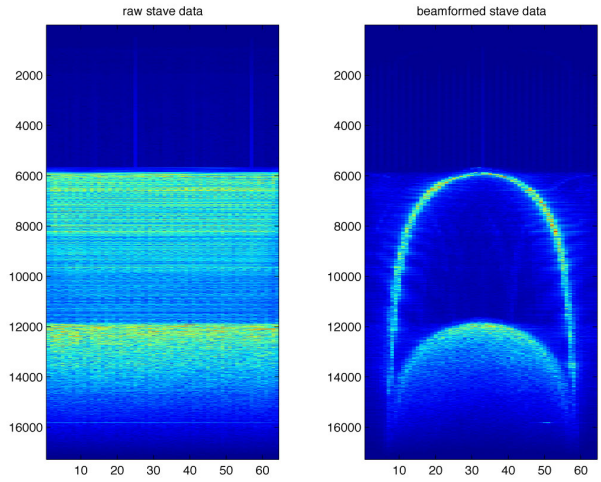

Figure 12: (left) Reflected sonar amplitude versus time (increasing down) and stave number (across). This example comes from an EM120 with 64 staves. The range sampling rate is 2 kHz. (right) Beam formed stave data where the horizontal axis now corresponds to the sine of the look angle.

Table 2: Sectors and frequencies (Hz) for the Kongsberg EM122.

Port				Center	Starboard			
1	3	5	7	9	8	6	4	2
11550	12150	12600	11850	12450	11400	12300	11700	11250

of each ping is 67 Hz corresponding to a pulse length of 15 ms and a range resolution of 11.25 m. For shallower depth the bandwidth is increased to 200 Hz corresponding to a range resolution of 3.75 m.

After this pre-processing of the columns into unique look angles, a bottom detection algorithm is used to measure the two-way travel time and thus the range for each beam. Then the cross-track depth profile can be estimated from the look angle and range as shown in Figure 3.

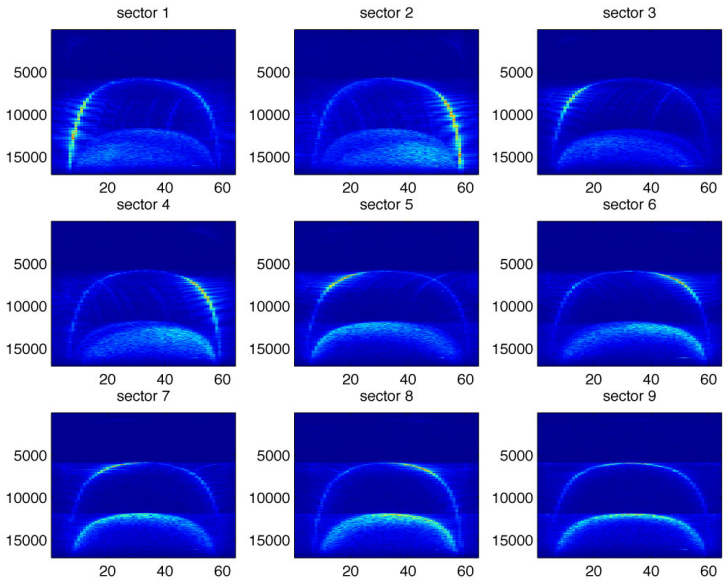

Figure 13: Stave data is first divided into sectors by frequency filtering in time (columns) and then beam formed by Fourier Transform of rows.

7 Roll, Pitch, and Yaw Compensation

As discussed in the introduction a major challenge of measuring depth from a ship is that the ocean waves cause the platform to be constantly rotating in all three directions. The geometry of the three important angles is shown in in Figure 14. An example of a time series of pitch, roll, and heave is provided in Figure 15. In this case the roll angle was more than 10 degrees. If this was not corrected it would result in a depth error of more than 1 km on the outermost beam at 7 km from the nadir trackline. Achieving better than 10 m of depth error on the outermost beam requires an accuracy of 0.08°. Therefore accurate bathymetry requires an accurate roll correction.

The sonar provides a real-time correction for pitch and roll angles using a vertical reference unit (VRU) that can record off vertical angles to about 0.01° accuracy. The transmit array ensonifies a narrow beam (about 1°) in the along-track direction. A pitch error of greater than about 0.5° will place the footprint in the wrong location ultimately blurring the seafloor map. The

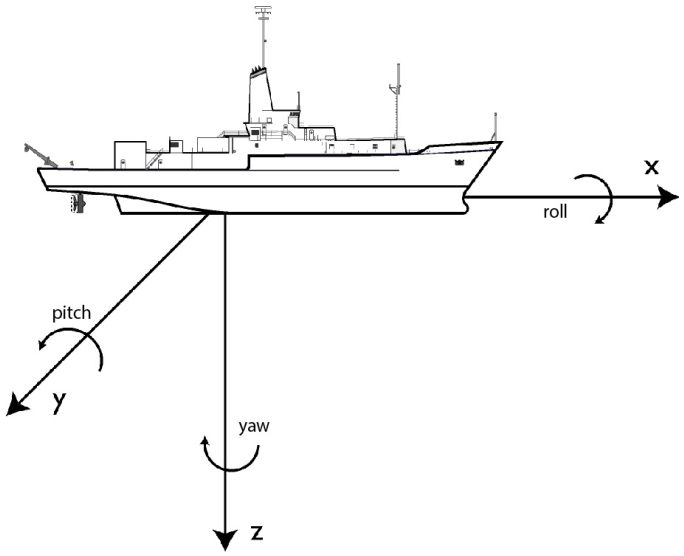

Figure 14: Geometry of roll, pitch, and yaw angles for a ship.

problem is corrected in real time. First the VRU records the pitch and roll angles at a sampling rate of 10 Hz. Then the current pitch angle is sent to the sonar where a pitch correction is applied to the transmit array to correct for this angle. The correction to the roll angle can be performed in real time although it can also be done in post processing. Again the roll angle from the VRU is used by the sonar to correct the incidence angle relative to the true vertical. Note that since the return pulse must be recorded for several seconds, the roll correction will be time dependent. This section provides only a conceptual description of these corrections. The engineering behind this rather complicated system is marvelous and sophisticated and beyond the scope of this document.

8 Effects of the Sound Speed Profile

Our analysis thus far has assumed a uniform speed of sound C_d in the water column, from which the beam steering is calculated. In the real world, the sound speed varies as a function of temperature and salinity, both of which change with depth. As a result, locations of depth soundings will be improperly estimated because they arrive at slightly different look angles compared

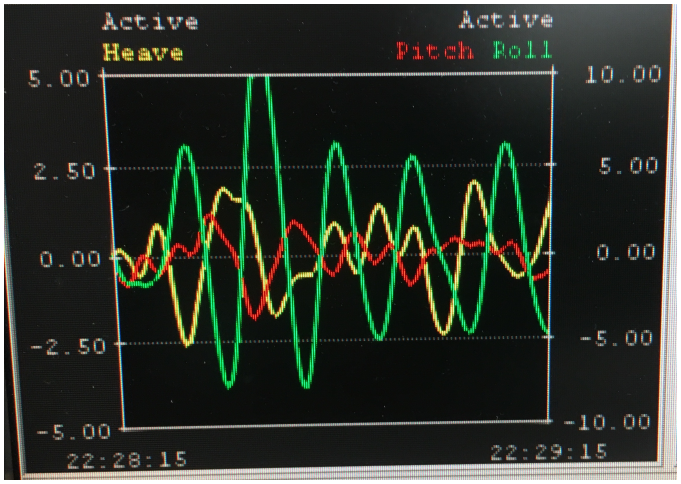

Figure 15: Time series of pitch and roll for 1 minute. Right vertical axis is in degrees.

to $\theta_d = \theta_{beam} + \theta_{roll}$ predicted by the beam steering and roll compensation, which is calculated with C_d.

A strategy to address this is detailed in de Moustier [1988]. In principle, the depth H of a point on the seafloor may be calculated as $H(\theta) = \rho \cos\theta = \frac{C_d}{2} t \cos\theta$, where t is the travel time and ρ is the slant range. There are two ways in which this may be modified due to perturbations in the sound speed profile. In the simpler case, the sound speed C_d is accurate except for some sound speed perturbation at the sea surface that may be measured during transit. In this case, the slant range is not affected but the apparent look angle will be bent according to Snell's Law:

$$\frac{\sin\theta'}{C'} = \frac{\sin\theta_d}{C_d} \tag{13}$$

As a result, the apparent depth profile is distorted to

$$H'(\theta) = \frac{C_d}{2} t \cos\left(\mathrm{Sin}^{-1}\left[\frac{C'}{C_d}\sin\theta\right]\right). \tag{14}$$

We estimate the effect of this distortion in Figure 16, which shows the normalized water depth calculated when the surface sound velocity changes by $\pm 6.6\%$, the maximum theoretical change that could result from moving

from polar to tropical latitudes [de Moustier, 1988]. The difference between true and distorted look angles increases for greater angles, causing greater errors for outer beams.

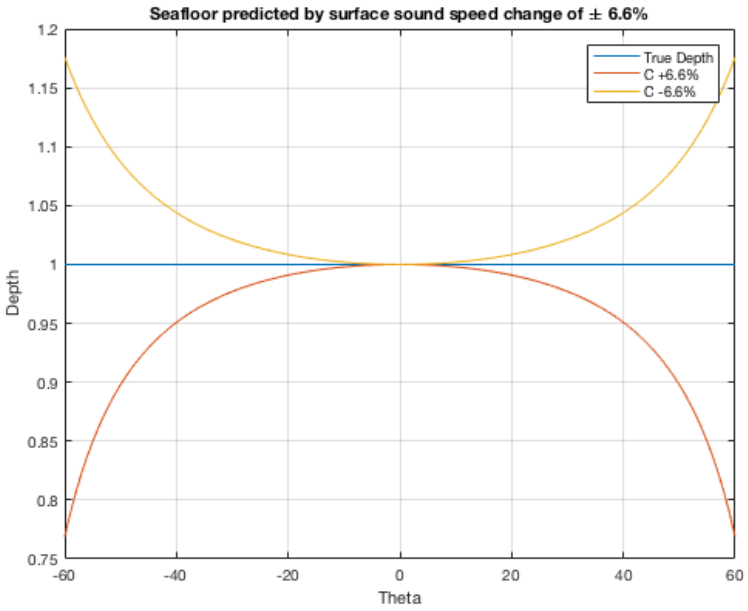

Figure 16: Normalized depth change from a change in surface sound velocity.

In addition, there is a possibility that the default sound speed used throughout the profile is wrong, which will affect both the slant range and look angle. The strategy to address this is to compute the average speed of sound by integrating sound speed across the vertical water column:

$$C_{avg} = \frac{1}{H_0} \int_0^{H_0} C(z)dz \tag{15}$$

The change in water depth due only to the change in slant range in shown in Figure 17. Curiously, changing the range, only shifts the depth values up or down by a constant, due to the range and depth increasing linearly with sound speed.

After computing C_{avg}, the true look angle of a depth sounding may be estimated once again using Snell's Law:

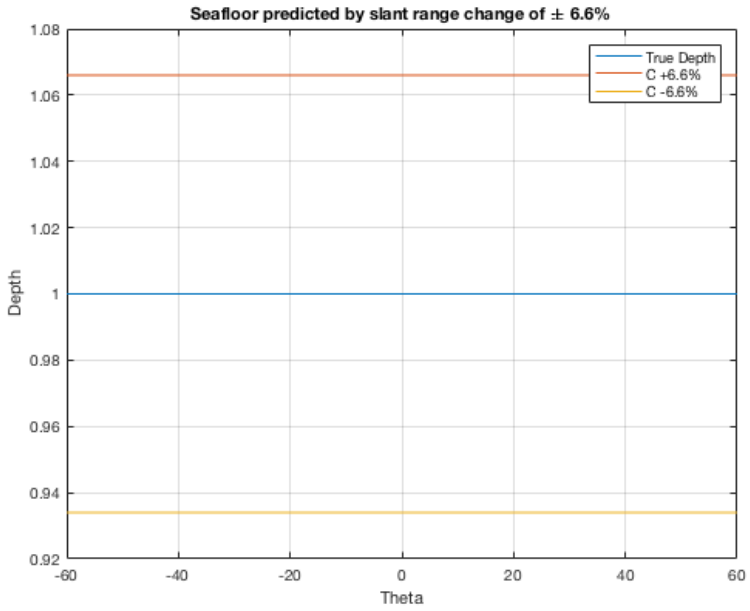

Figure 17: Normalized change in water depth due to a range change of ±6.6%.

$$\frac{\sin\theta_{true}}{C_{avg}} = \frac{\sin\theta'}{C'} \tag{16}$$

In this case, the new depth profile would be calculated by replacing C_d with C_{avg} and θ with θ_{true} in our initial expression for $H(\theta)$. Figure 18 synthesizes both the distortions to the look angle and range due to changing the average sound speed.

One final note is that de Moustier [1988] recommend using the harmonic mean:

$$C_h = \left[\frac{1}{H_0}\int_0^{H_0}\frac{dz}{C(z)}\right]^{-1} \tag{17}$$

which they claim yields preferable results to the standard mean.

Of course, this processing technique relies on the user obtaining an accurate sound speed profile. This may be done by deploying an expendable bathythermograph (XBT). However, maintaining an accurate sound speed profile during a cruise can prove difficult because of shallow depth internal

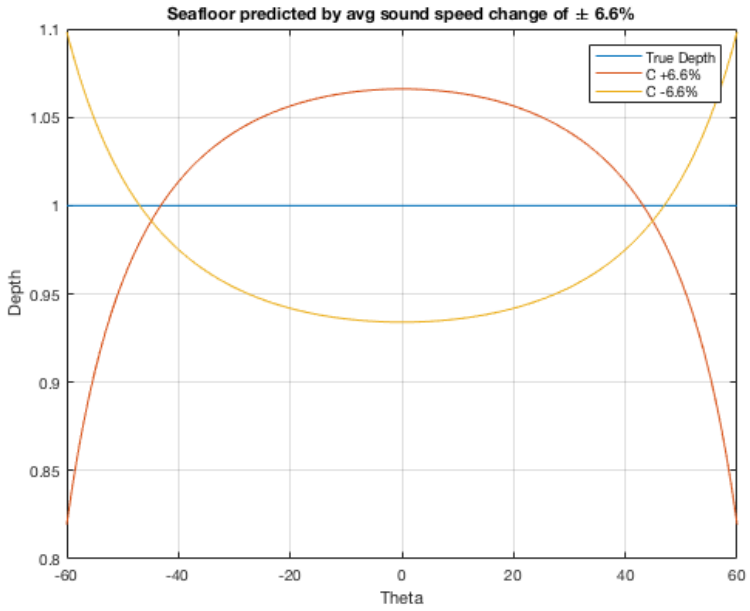

Figure 18: Change in normalized water depth due to a ±6.6% change in average sound speed.

waves that may alter the sound speed over timescales of tens of minutes to hours. We will discuss how to address these sound speed errors in a later section.

9 Sidescan Sonar

Thus far we have considered depth measurements collected by the multibeam sonar, but the instrument is also capable of collected information based upon the amplitude of the returned pulse. This information is referred to as backscatter or sidescan sonar, the latter name arising from sonars employed before the advent of multibeam systems. As before, the physics behind sidescan sonar are very similar to those behind satellite radar, so the following notes are partially adapted from the Rees [2013] treatment of electromagnetic radiation, as well as the SeaBeam Theory of Operation notes.

Start by considering a flat, uniform seafloor. A transmitter at the sea

surface emits a pulse and measures the echoes from the seafloor, as was the case for multibeam. However, this time we are interested in the entire time series of amplitude vs time for the returning pulse. For a featureless seafloor, we expect the peak amplitude of the returned pulse to occur at the first return; subsequent amplitudes will steadily decrease as governed by attenuation in the water column since they have travelled slightly longer distances. When the seafloor is non-uniform, the amplitude of the sonar echoes will deviate from uniform seafloor case depending on whether or not the energy is being reflected by a smoother or rougher patch of seafloor. Thus, we may use these echoes to characterize the roughness of the area ensonified by the ping.

There are a few shortcomings in our analysis thus far. First, we need some way of determining whether the echoes are returning from the port or starboard side of the ping. This is accomplished by considering the different pulse frequencies utilized to ensonify to different beam sectors (Figure 13, Table 2) to create two time series, one each for the echo amplitudes reflecting from the port and starboard sides of the vessel. (Incidently, this is also how the name "sidescan" came into usage.)

We also need some way of locating the echoes in space, which we do by estimating the slant range to each point. A simple way to do this is by converting from the time difference between the outgoing and returning pulses, ie $\rho = \frac{Ct}{2}$ where ρ is the slant range, C is the speed of sound, and t is time. With an estimate of slant range, we may locate the points in space depending on the shape of the seafloor. For the case of a flat seafloor, the minimum range ρ_0 occurs at vertical incidence and each range value corresponds to a unique look angle $\theta = \cos^{-1}(\rho_0/\rho)$.

10 Range Resolution

The sonar emits a short pulse that reflects off the seafloor and returns to the hydrophone array. The amplitude vs time of the return pulse is a recording of the reflectivity of the seafloor. If adjacent reflectors appear as two distinct peaks in the return waveform then they are resolved in range. The nominal slant range resolution is $\Delta r = C\tau/2$ where τ is the pulse length, and C is the speed of sound in seawater. The factor of 2 accounts for the two-way travel time of the pulse.

References

Michael A Ainslie and James G McColm. A simplified formula for viscous and chemical absorption in sea water. *The Journal of the Acoustical Society of America*, 103(3):1671–1672, 1998.

JJ Becker, DT Sandwell, WHF Smith, J Braud, B Binder, JL Depner, D Fabre, J Factor, S Ingalls, SH Kim, et al. Global bathymetry and elevation data at 30 arc seconds resolution: Srtm30_plus. *Marine Geodesy*, 32(4):355–371, 2009.

Ronald Newbold Bracewell. *The Fourier transform and its applications*, volume 31999. McGraw-hill New York, 1986.

Christian de Moustier. State of the art in swath bathymetry survey systems. 1988.

Harold K Farr. Multibeam bathymetric sonar: Sea beam and hydro chart. *Marine Geodesy*, 4(2):77–93, 1980.

Kongsberg. EM 120 12 kHz multibeam echo sounder, 2011.

William Gareth Rees. *Physical principles of remote sensing*. Cambridge university press, 2013.